PHASE EVOLUTION IN AND CREEP PROPERTIES OF NB-RICH NB-SI-CR EUTECTICS

Florian Gang, Alexander Kauffmann, Martin Heilmaier

Institute for Applied Materials (IAM-WK), Karlsruhe Institute of Technology (KIT), Engelbert-Arnold-Str. 4, D-76131 Karlsruhe, Germany

corresponding author: Florian Gang, florian.gang@kit.edu

This manuscript is intended for publication in the MMTA special issue on the “TMS 2017 Materials for High Temperature Applications: Next Generation Superalloys and Beyond” symposium.

Abstract

In this work, the Nb-rich ternary eutectic in the Nb-Si-Cr system has been experimentally determined to be Nb-10.9Si-28.4Cr (in at.%). The eutectic is composed of three main phases, Nb solid solution (Nb_{ss}), β-Cr_2Nb and $Nb_9(Si,Cr)_5$. The ternary eutectic microstructure remains stable for several hundred hours at a temperature up to 1200 °C. At 1300 °C and above, the silicide phase $Nb_9(Si,Cr)_5$ decomposes into α-Nb_5Si_3, Nb_{ss} and β-Cr_2Nb. Under creep conditions at 1200 °C, the alloy deforms by dislocation creep while the major creep resistance is provided by the silicide matrix. If the silicide phase is fragmented and, thus, its matrix character is destroyed by prior heat treatment (e.g. at 1500 °C for 100 h), creep is mainly controlled by the Laves phase β-Cr_2Nb, resulting in increased minimum strain rates. Compared to state of the art Ni-based superalloys, the creep resistance of this three phase eutectic alloy is significantly higher.

Keywords: eutectic alloys, niobium silicides, intermetallics, refractory based alloys, creep

I. Introduction

Due to their high melting point and relatively low density, Nb-Si based alloys are promising novel materials for high temperature structural applications [1, 2]. Unfortunately, good mechanical strength and oxidation resistance at elevated temperatures, as well as sufficient fracture toughness at ambient temperature, are difficult to achieve simultaneously in a satisfactory manner, as the improvement of one property usually comes along at the expense of the other. This challenge may be met by e.g. combining different phases with complementary properties in a fine eutectic microstructure. For example, in the Nb-Si binary system, the binary eutectic Nb-18Si (in at.%) showed a combination of high creep strength subsequent to directional solidification [3] with reasonable fracture toughness [4] due to the presence of the silicide and Nb solid solution (Nb_{ss}), respectively. However, this alloying system did not provide acceptable oxidation resistance, as the bulky, porous and non-adherent oxide Nb_2O_5 is formed. Hence, further alloying additions are necessary to suppress the formation of Nb_2O_5. For example, Ti, Al, Sn and Cr are known to increase the oxidation resistance [5–8]. However, only the system Nb-Si-Cr features a Nb-rich ternary eutectic as a prerequisite for later directional solidification.

For this reason, the model system Nb-Si-Cr was selected, where Cr is added to mainly improve the oxidation resistance, by replacing the fast forming, bulky, non-adherent oxide Nb_2O_5 by dense, adherent $CrNbO_4$ scales [9]. Si is known to improve the creep properties by formation of silicide phases while Nb solid solution (Nb_{SS}) provides suitable fracture toughness. However, a literature survey reveals contradictory information on the exact composition of the ternary eutectic in this system. In 2005, Shao calculated the ternary eutectic composition to be Nb-12Si-25Cr [10] (in at.%) using CALPHAD. In contrast, Bewlay et al. experimentally assessed the Nb-Si-Cr system in 2009 to determine the ternary eutectic composition to be close to Nb-8.7Si-33.1Cr [11]. Therefore, the exact location of the ternary eutectic is critically reviewed in this study with samples of different appropriate alloy compositions produced by arc melting. The identified composition of the ternary eutectic is thoroughly assessed in terms of phase evolution, as well as microstructure and phase stability. Moreover, the creep behavior at the potential operating temperature of 1200 °C is assessed.

II. Experimental

To determine the ternary eutectic composition, different alloys were synthesized from elemental granules (Cr, purity 99,0 wt.%; Si purity 99,9999 wt.%) and slug (Nb, purity 99,8 wt.%) using an arc melter AM/0.5 (Edmund Buehler GmbH, Hechingen, Germany) with tungsten electrode. Chemical analysis of cast ingots (mass 30 g) was carried out by means of inductively coupled plasma optical emission spectrometry (ICP-OES). For heat treatments and microstructure examinations, the ingots were cut into smaller pieces using electro discharge machining. Heat treatments were performed in a high temperature furnace Gero HTRH 70-600/18 (Carbolite Gero GmbH, Neuhausen, Germany) under Ar atmosphere. Metallographic samples were hot-mounted in “Duroplast” resin (ATM GmbH, Mammelzen, Germany) using a Simplimet 1000 (Buehler, Lake Bluff, IL, USA), prior to grinding using SiC paper with successively decreasing particle size and finally polished with a diamond suspension. To prepare samples for electron backscatter diffraction (EBSD), two additional semiautomatic polishing steps with both non-crystallizing, pH-neutral OPS (10 minutes) and alkaline stabilized OPS (1 minute) were performed to remove remaining surface-near plastic deformation by the prior polishing steps.

The microstructure was examined using an SEM EVO 50 (Carl Zeiss AG, Oberkochen, Germany) in backscattered-electron mode (BSE) to reveal the different phases. Phase fractions (vol.%, as material is expected to be isotropic) were determined on at least five SEM-BSE images each using the software ImageJ for quantitative image analysis by threshold segmentation. Local phase compositions were determined applying electron probe micro analysis (EPMA). Either the aforementioned SEM was used for standardless energy-dispersive spectroscopy (EDS) measurements or a SEM JEOL JXA-8100 (JEOL GmbH, Freising, Germany) was employed for wavelength-dispersive spectroscopy (WDS) measurements using the standards J13_Cr, J13_Si, J13_ZrO_2 and 9033Nb. EBSD was performed using an EDAX DigiView camera on a Zeiss Auriga 60 SEM (Carl Zeiss AG, Oberkochen, Germany). For analysis of the determined EBSD patterns, a commercial software provided by EDAX was used. Creep tests on cuboidal samples (size 3 mm x 3 mm x 5 mm) were performed in compression in an electro-mechanical universal testing machine Zwick Z100 (Zwick GmbH, Ulm, Germany) with attached vacuum furnace (Maytec GmbH, Singen, Germany) at constant true stress at 1200 °C in vacuum. All creep experiments were terminated before failure of the samples.

III. Results and Discussion

Determination of the ternary eutectic

Figure 1 compares the microstructures of the two different ternary eutectic compositions suggested in the literature [10,11]. It becomes obvious that Nb-12Si-25Cr (Figure 1a) is not a ternary eutectic, as a significant amount of primary solidifying Nb_{ss} (light-grey phase, phase fraction (25.1 ± 3.2) vol.%) is located between a subsequently solidified two-phase eutectic microstructure. According to EDS measurements, this eutectic consists of Nb_{ss} and a ternary silicide phase in the compositional range of $Nb_9(Si,Cr)_5$ (grey phase). However, at equilibrium, α-Nb_5Si_3 silicide is expected according to calculations by Shao [10]. The determined $Nb_9(Si,Cr)_5$ silicide composition matches quite well with the one reported by Bewlay et al. for the phase present in the vicinity of the ternary eutectic [11]. This mismatch between calculation and experiment might be due to an incomplete Calphad database, in which the ternary silicide has not been implemented. Despite of some Cr-rich segregations (dark grey phase), no other phases are detectable in Figure 1a.

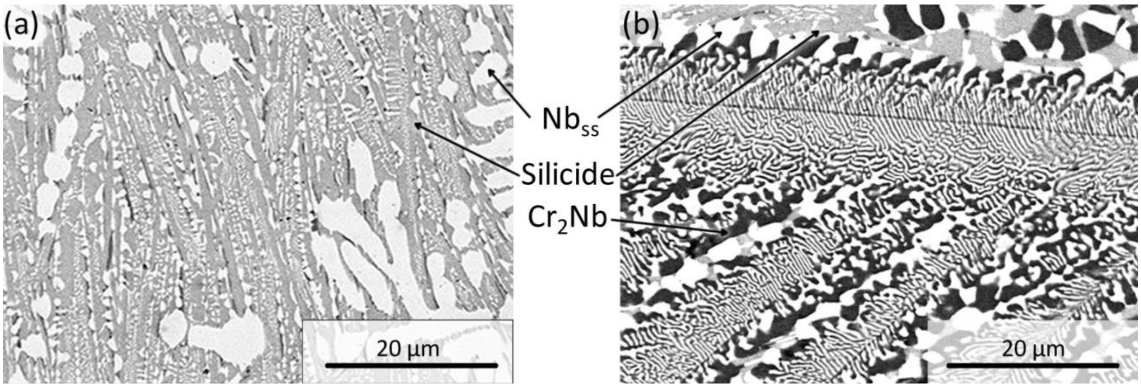

Figure 1: SEM-BSE micrographs of the alloys (a) Nb-12Si-25Cr and (b) Nb-8.7Si-33.1Cr, both in as cast condition

In contrast, the second proposed composition Nb-8.7Si-33.1Cr, shown in Figure 1b, does not exhibit primary solidification of a single phase, indicating close proximity to the ternary eutectic composition. The microstructure is characterized by two distinct features:

(i) very fine two-phase lamellar eutectic cells, in which a coupled growth of Nb_{ss} (white phase) and Cr_2Nb (dark-grey phase) occurs;

(ii) in between, coarse regions consisting of three different phases, i.e. Nb_{ss} (white phase), Cr_2Nb (black phase) and a third undetermined silicide phase (light-grey).

This ternary phase does not correlate with the compositional range of $Nb_9(Si,Cr)_5$, as its chemical composition was determined to be (50.2 ± 0.5) at.% Nb,(15.2 ± 0.2) at.% Si and (34.6 ± 0.3) at.% Cr, which does not match with any known phase in the Nb-Si-Cr system. However, the identification and the study of this unknown phase are beyond the scope of the present study and will not be addressed hereafter. Therefore, Nb-8.7Si-33.1Cr is also not the exact ternary eutectic composition.

To reduce the gap between literature results and experiments regarding the ternary eutectic composition, a triangulation scheme was carried out by examining compositions in the vicinity of Nb-8.7Si-33.1Cr. Starting from this composition, either the Si or Cr content was varied to achieve primary solidification of either Nb_{ss} or Cr_2Nb. The examined compositions are given in Table 1 and are additionally plotted in the partial liquidus projection in Figure 2. Comparison between nominal composition and actual composition reveals no deviation within the range of the measurement uncertainty (standard deviation SD ≤ 0.4 at.% for Si, and SD ≤ 0.45 at.% for Cr). For this reason, only nominal compositions will be used in the following.

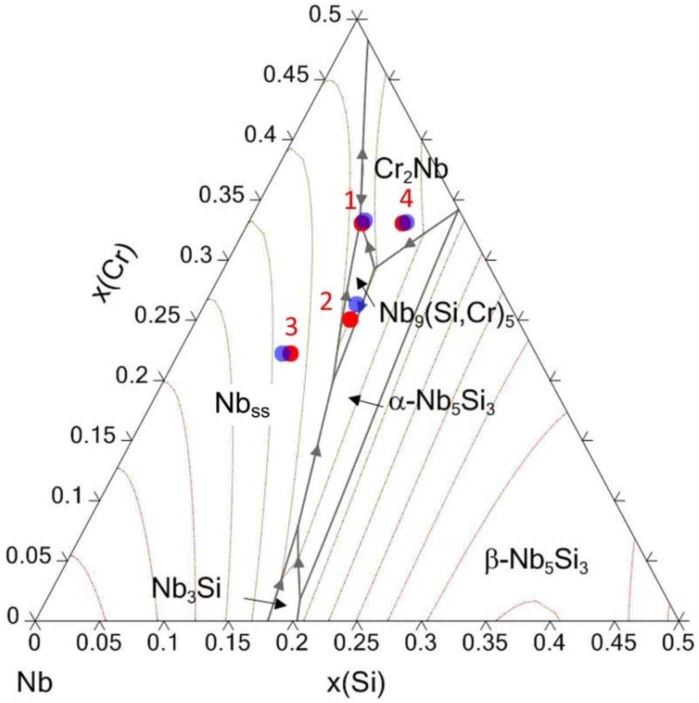

Figure 2: Partial liquidus projection of the Nb-Si-Cr system, including isothermal lines (calculated with PANDAT employing the PanNb database). Compositions according to the numbers are listed in Table 1. The red dots symbolize the nominal composition; blue ones represent the actual composition.

The microstructures of Alloys 1 (Nb-8.7Si-33.1Cr) and 2 (Nb-12Si-25Cr) have already been discussed. For Alloy 3 (Nb-8.7-22Cr), Nb$_{ss}$ primary solidification is expected. Indeed, growth of Nb$_{ss}$ primary dendrites (white phase) is visible in Figure 3a with a phase fraction of (36.6 ± 2.2) vol.%. Moreover, ternary eutectic is present, comprising Nb$_{ss}$, Cr$_2$Nb and Nb$_9$(Si,Cr)$_5$.The expected binary eutectic, which according to Figure 2 should consist of Nb$_{ss}$ and Nb$_9$(Si,Cr)$_5$, cannot clearly be separated from the ternary eutectic. Occasionally, binary eutectic structures of Nb$_{ss}$ + Cr$_2$Nb and Cr$_2$Nb + Nb$_9$(Si,Cr)$_5$ can be observed, which are not likely to form along the expected solidification path in equilibrium and may be attributed to segregation effects during solidification.

Conversely, Alloy 4 (Nb-12Si-33-1Cr), is expected to solidify from the Cr$_2$Nb phase region. This feature is confirmed in Figure 3b, where Cr$_2$Nb dendrites (black phase) are identified, having a phase fraction of (23.6 ± 0.6) vol.%. Adjacent to primary dendrites, the binary eutectic Nb$_{ss}$ + Cr$_2$Nb is formed. Subsequently, the remaining melt solidifies by formation of ternary eutectic cells.

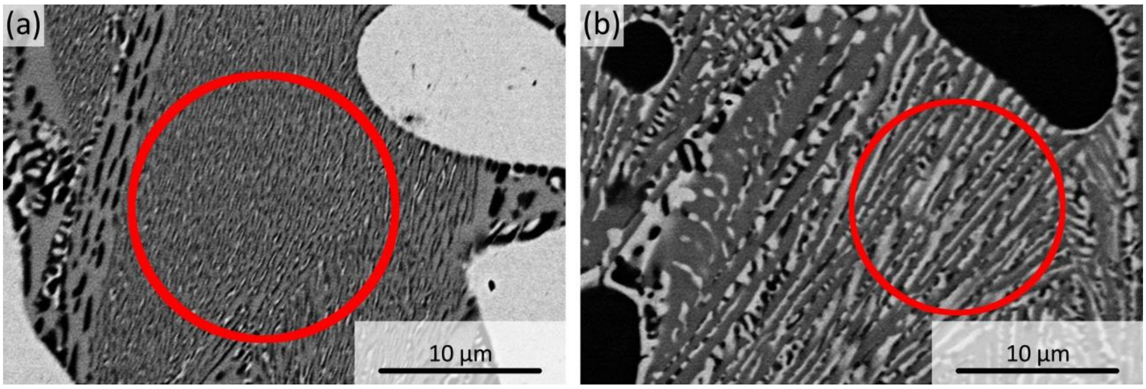

Figure 3: SEM-BSE micrographs of the alloys (a) Nb-8.7Si-22Cr and (b) Nb-12Si-33.1Cr. In both alloys ternary eutectic structures can be observed (marked with a red circle).

To determine the chemical composition of the ternary eutectic, EDS area scans of eutectic cells have been performed on Alloys 3 and 4. Exemplarily analyzed regions are marked by red circles in Figure 3. Quantitative results for these scans are given in Table 2. The compositions for eutectic cells in both alloys are very similar. Accordingly, the “true” ternary eutectic composition has been approximated as Nb-10.9Si-28.4Cr. This seems to be confirmed by the micrographs in Figure 4, where the microstructure of an alloy with actual composition of Nb-10.8Si-28.8Cr consists almost entirely of ternary eutectic cells. Within these cells, the silicide phase $Nb_9(Si,Cr)_5$ forms a discontinuous matrix (phase fraction (67.7 ± 4.2) vol.%), which is clearly underlined by Figure 4c and orientation analysis that reveal uniform orientation of $Nb_9(Si,Cr)_5$ within the colonies. Between this silicide matrix, Nb_{ss} and Cr_2Nb grow in a coupled manner with phase fractions of (14.6 ± 4.7) vol.% and (17.7 ± 4.9) vol.%, respectively. Distributed along the cell boundaries, coarse regions of $Nb_9(Si,Cr)_5$ and the binary eutectic Nb_{ss} + Cr_2Nb are present, which must have solidified before the ternary eutectic. As this slightly off-eutectic solidification occurs along the cell boundaries, the ternary eutectic composition was double-checked within the cells and the composition Nb-10.9Si-28.4Cr was confirmed. Chemical compositions of each individual phase were measured using WDS on the coarse regions. The results are given in Table 3. The actual chemical composition of Nb_{ss} is in good agreement with previously published solubility limits of Si (2.4 at.%) and Cr (16.0 at.%) in an isothermal section at 1500 °C of the Nb-Si-Cr system [12]. For $Nb_9(Si,Cr)_5$, the measured composition is close to the stoichiometry of the phase.

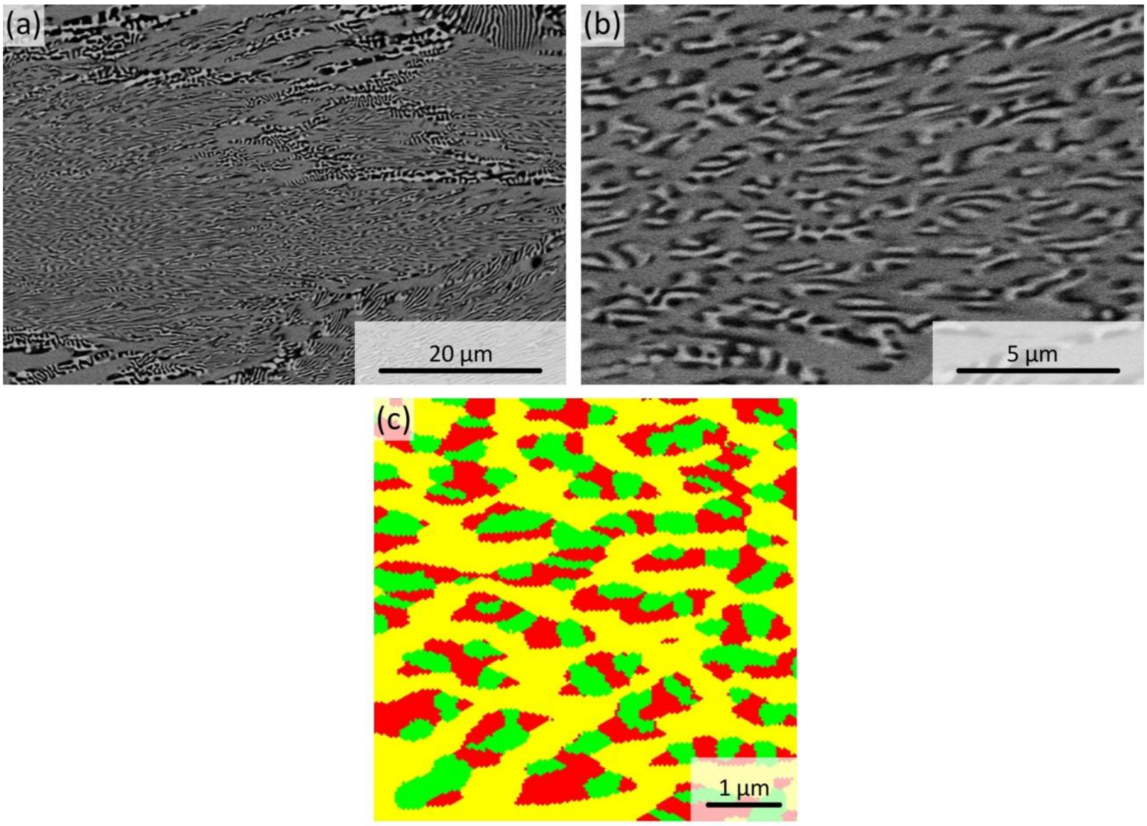

Figure 4: Micrographs of the ternary eutectic alloy Nb-10.9Si-28.4Cr: (a-b) SEM-BSE mode and (c) EBSD, false-color image of the phases $Nb_9(Si,Cr)_5$ (yellow), Nb_{ss} (green) and Cr_2Nb (red).

In Cr_2Nb, Si is significantly substituting for Cr. According to Ref. [13], up to 26 at.% of Si can substitute Cr, stabilizing the hexagonal high temperature modification β-Cr_2Nb (C14, hP12, $P6_3/mmc$) down to ambient temperature. In contrast, the hexagonal, binary β-Cr_2Nb phase would transform into its cubic low temperature modification α-Cr_2Nb (C15, cF24, Fd3m) below 1600 °C for the binary Nb-Cr system [14]. The presence of β-Cr_2Nb in Nb-10.9Si-28.4Cr was additionally confirmed using EBSD; indexed diffraction patterns for all phases present in Nb-10.9Si-28.4Cr are shown in Figure 5. For the sake of simplicity, Cr_2Nb will refer to the β-Cr_2Nb phase in the following.

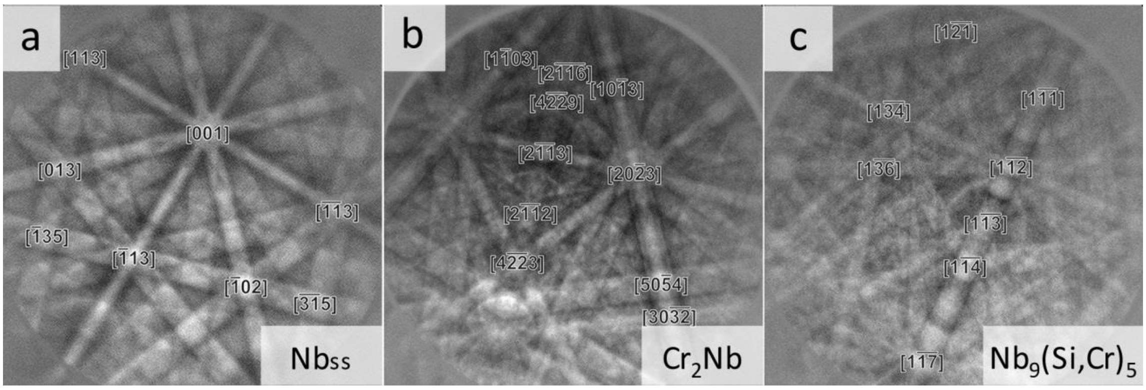

Figure 5: Indexed EBSD patterns of the phases present in Nb-10.9Si-28.4Cr: (a) Nb_{ss}, (b) Cr_2Nb and (c) $Nb_9(Si,Cr)_5$.

Phase stability

For high temperature applications, microstructural as well as phase stability at and above service temperature is a crucial requirement. Therefore, the evolution of microstructural parameters such as phase fraction and size was examined after exposure to high temperatures. Besides long term stability (500 h) at 1200 °C which may be a potential operation temperature for turbine applications higher temperatures (1300 °C and 1500 °C) were also considered for shorter periods of time (100 h). Figure 6 shows the microstructure of Nb-10.9Si-28.4Cr in the as cast state as well as after such heat treatments. It is complemented by Figure 7 which illustrates the corresponding phase fractions and sizes.

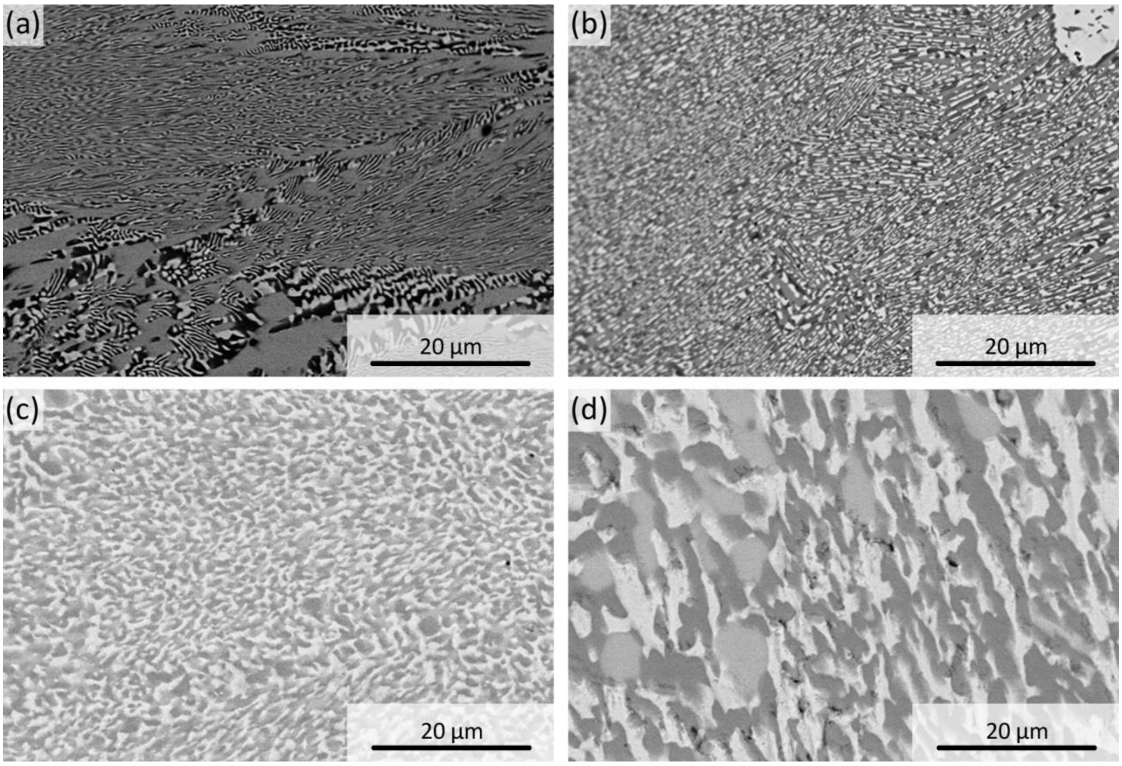

Figure 6: Phase evolution and stability in the alloy Nb-10.9Si-28.4Cr, starting from as cast state in (a) for different heat treatment conditions: (b) 1200 °C, 500 h; (c) 1300 °C, 100 h and (d) 1500 °C, 100 h.

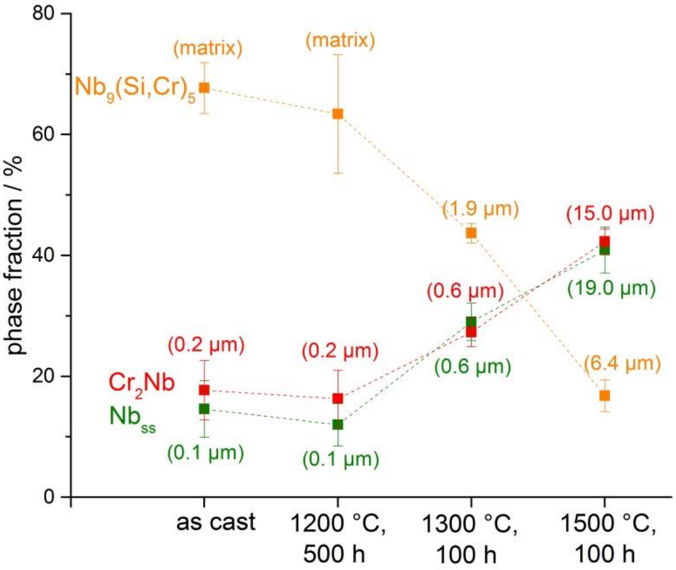

Figure 7: Evolution of phase fraction and -size in Nb-10.9Si-28.4Cr for different heat treatment conditions. Average phase size determined by segmentation of BSE images is provided in brackets. Connecting lines are to guide the eyes.

Compared to the as cast state, homogenization of the microstructure occurs for all heat treatment conditions. The inhomogeneous boundaries of the eutectic cells disappear. Apart from homogenization, the microstructure remains stable for up to 500 h at 1200 °C. At 1300 °C, slight coarsening of the phases is observed. The phase fraction of $Nb_9(Si,Cr)_5$ decreases significantly, while the amounts of Nb_{ss} and Cr_2Nb increase simultaneously and uniformly. Moreover, the silicide phase loses its matrix character. These effects are even more pronounced at 1500 °C. Hence, the examined alloy undergoes profound morphological changes during heat treatments. Especially the pronounced decrease of the silicide phase fraction and the simultaneous increase of Nb_{ss} and Cr_2Nb fractions are worth mentioning. As this effect might result from possible phase transformations, the local chemical composition was checked again after heat treatments. Results subsequent to annealing at 1500 °C for 100 h are shown exemplarily in Table 4. Even though slight compositional variations have occurred in Nb_{ss} and Cr_2Nb, these two phases are still present after heat treatment. In contrast, the silicide phase shows a significant change in terms of chemical composition. The Si content is increased to about 38 at.% (as compared to roughly 16 at.% in the as cast state). However, the Cr content has been reduced dramatically (1.5 at.% as compared to 21 at.%). Thus, the stoichiometry of the silicide phase hints for the presence of Nb_5Si_3 instead of $Nb_9(Si,Cr)_5$ after heat treatment. EBSD diffraction patterns presented in Figure 8 reveal that the silicide phase identified is the tetragonal α-Nb_5Si_3 (tI32, I4/mcm [15]). Figure 8b demonstrates that this evolution into α-Nb_5Si_3 is already active at temperatures as low as 1300 °C.

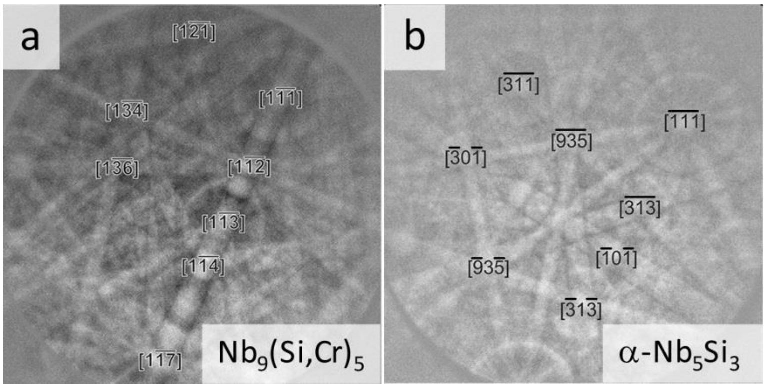

Figure 8: indexed EBSD diffraction patterns showing the silicide phase evolution in Nb-10.9Si-28.4Cr for different heat treatment conditions: (a) $Nb_9(Si,Cr)_5$ in as cast state and (b) α-Nb_5Si_3 after 1300 °C, 100 h

Attempts to address this solid-state reaction, e.g. by DSC measurements, were not successful so far. Nevertheless, as the transformation from $Nb_9(Si,Cr)_5$ to α-Nb_5Si_3 coincides with increasing phase fractions of Nb_{ss} and Cr_2Nb, a eutectoid-like decomposition is conceivable. A eutectoid decomposition is already known from the Nb-Si binary system, where Nb_3Si decomposes into Nb_{ss} and α-Nb_5Si_3 at 1763 °C [16]. However, this solid-state reaction follows very slow kinetics [17], where a full eutectoid decomposition of Nb_3Si cannot be achieved even after 1500 °C for 500 h [18]. Hence, the absence of distinct reaction peaks during DSC measurements (not shown here) is not uncommon.

Creep properties

For high temperature applications, considerable slow creep deformation under constant load at homologous temperature $T/T_m > 0.4$, where T_m is the melting temperature, is one of the major design criteria for structural applications.

From previous results, the microstructure of the ternary eutectic appears to be stable in terms of phase fraction and size for temperatures up to 1200 °C, which might be a potential service temperature. Therefore, compressive creep tests were performed at this temperature on as cast material. The evolution of strain rate in dependence of true plastic strain is shown in Figure 9a. As soon as constant true stress was applied, a decrease in strain rate indicates initial strain hardening. This effect is more pronounced with decreasing true stress. The strain rates decrease until a minimum strain rate is reached at about 1 % true plastic strain, which is similar for all true stresses tested. Immediately following the minimum, the strain rate slowly but continuously increases. Therefore, a stationary or so called “steady state” creep region where a dynamic equilibrium between strain hardening and recovery is established cannot be determined. Instead, a minimum creep rate has been defined at 1% plastic strain and is marked with red dots in Figure 9a. As true stress is applied in compression throughout the experiments and no significant microstructural changes were observed during creep (not shown here since similar to load-free heat treatment), only internal damage, e.g. cracking within the silicide or along the phase boundaries can cause the observed absence of stationary creep. This has already been reported by Bewlay et al. [19] and Seemueller et al. [20]. Even though cracking of the silicide, being still brittle at the temperature tested, is the most likely explanation for the observed effect, no significant damage could be observed, as the total strain achieved was < 2 % and therefore very small.

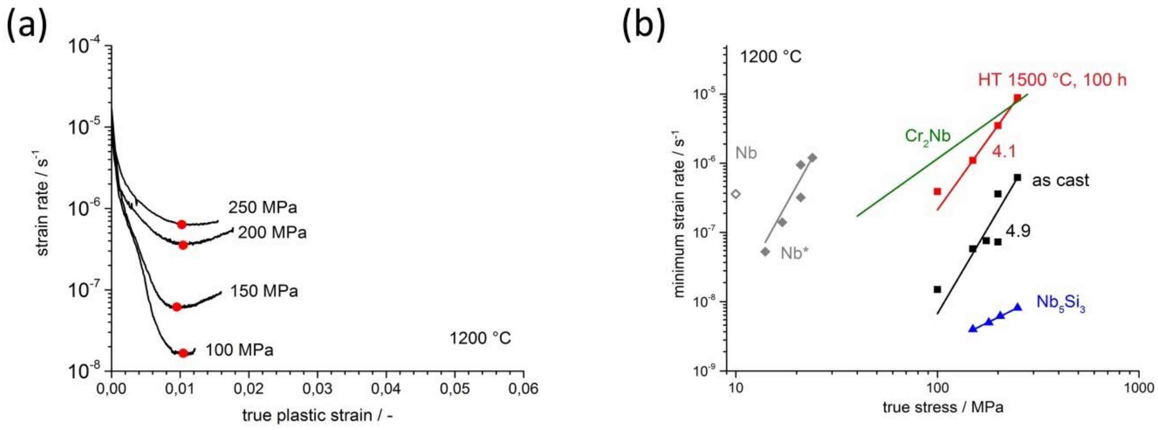

Figure 9: Stress dependence of the strain response for Nb-10.9Si-28.4Cr, shown as (a) strain rate vs. true plastic strain (deliberately stopped subsequent to minimum) and (b) minimum strain rate vs. true stress (Norton plot). Data marked with "*" were determined at 1000 °C.

The Norton plot in Figure 9b depicts the minimum strain rate with respect to the applied true stress. For comparison, literature values of compressive creep data for monolithic Nb_5Si_3 [21] (as no literature data for $Nb_9(Si,Cr)_5$ is available), Cr_2Nb [19] and pure Nb [22] were added. Data for Nb-10.9Si-28.4Cr, heat treated at 1500 °C for 100 h are included as well since this microstructure should be stable at the testing temperature of 1200 °C.

Surprisingly, the as cast condition, which according to Figure 7 has a substantially lower phase size than the heat treated condition, exhibits the lowest creep rates. An explanation for this effect can be found in the matrix character of the silicide phase $Nb_9(Si,Cr)_5$ after casting (phase fraction of ≈ 68 %). This phase carries the load, supports the substantially less creep resistant phases Cr_2Nb and Nb_{ss} and thus controls the creep resistance in the former case. The mitigation of Nb_5Si_3 creep properties by Nb_{ss} using a rule of mixture approach could explain the intermediate position obtained for Nb-10.9Si-28.4Cr. Simulation based on such approach in binary Nb-Si alloys, consisting of Nb_{ss} and Nb_5Si_3, showing similar results, were already published [23, 24]. On the other hand, a difference in $Nb_9(Si,Cr)_5$ creep strength in the present alloy compared to monolithic Nb_5Si_3 may also explain strain rate variations.

Increased strain rates obtained for heat treated conditions could be attributed to the decreasing fraction of the silicide phase and the loss of its matrix character. This influence of the silicide phase fraction on the creep behavior has already been published in the literature for quaternary Nb-Si-Ti-Hf alloys [19]. The minimum strain rates shown in Figure 9b approach the values of the other phases involved in the microstructure, mainly the ones for Cr_2Nb. Due to the interpenetrating eutectic character of the microstructure, and since Nb_{ss} has no significant creep resistance at the present stress levels and temperature, the Laves phase Cr_2Nb carries the major part of load during creep and therefore determines the overall creep resistance of the alloy.

Stress exponents for both material conditions are in the order of magnitude expected for dislocation creep (n = 3 - 8). Supporting this finding, dislocation climb controlled creep has not only been reported in Nb and Cr_2Nb at temperatures above 1200 °C [25], but also for Nb_3Si [26]. Hence, the assumption of dislocation creep in the present silicide phase $Nb_9(Si,Cr)_5$ seems legitimate, even though no data for this monolithic phase are available.

Finally, the data obtained for Nb-10.9Si-28.4Cr are compared to compressive creep data for other refractory based silicides, as well as a state of the art Ni-based superalloy tested in tension, from the literature, in a density-normalized Norton plot in Figure 10, in order to critically assess the potential of the ternary eutectic alloy.

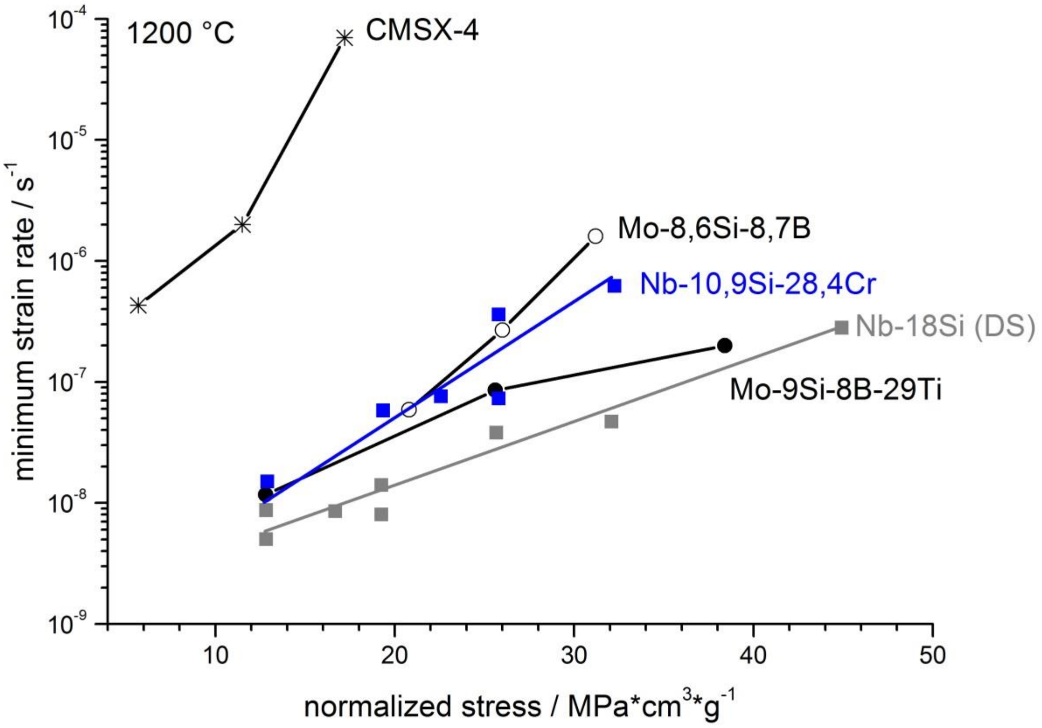

Figure 10: Density-normalized Norton plot, showing the potential of Nb-10.9Si-28.4Cr when compared to other refractory metals based alloys as well as Ni-based superalloys.

The minimum strain rates for Nb-10.9Si-28.4Cr are comparable with molybdenum silicides Mo-8.6Si-8.7B [27] and Mo-9Si-8B-29Ti [28] in the measurement uncertainty range. When compared to directionally solidified Nb-18Si [3], the fraction of load-bearing silicide phases is similar (≈ 66 % for Nb-18Si versus ≈ 68 % for Nb-10.9Si-28.4Cr). Hence the strain rate difference of one order of magnitude can be attributed to the phase alignment along the loading direction. Compared to the single-crystal Ni-based superalloy CMSX-4 [29], all refractory based alloys have up to two orders of magnitude lower strain rates. This is not surprising, as the testing temperature of 1200 °C is in the temperature range of γ' solvus in Ni-based superalloys, which leads to a significant loss of particle strengthening in these alloys.

IV. Conclusions

The chemical composition of the Nb-rich ternary eutectic in the system Nb-Si-Cr was experimentally determined to be Nb-10.9Si-28.4Cr. The phases present in the as cast state are Nb_{ss}, β-Cr_2Nb and $Nb_9(Si,Cr)_5$, the later forming an interpenetrating matrix. Microstructure and phase stability could be confirmed up to 1200 °C for several hundred hours. At this temperature, creep properties are comparable to other refractory based silicide alloys, dislocation controlled creep being the predominant mechanism. As compared to CMSX-4, significantly improved creep strength could be observed. However, above 1200 °C, the $Nb_9(Si,Cr)_5$ undergoes a presumably eutectoid-like decomposition into Nb_{ss}, β-Cr_2Nb and α-Nb_5Si_3. Because of this decomposition, Nb-10.9Si-28.4Cr loses its load-bearing $Nb_9(Si,Cr)_5$ matrix, which results in a significant loss of creep strength. Therefore the temperature limit for structural applications is currently set below 1300 °C. To overcome this limitation, more profound knowledge of the decomposition process is necessary. So far, employing available analyzing methods (e.g. DSC) could not yield information on both the exact transformation path and the reversibility of the process. Moreover, it has to be clarified, whether $Nb_9(Si,Cr)_5$ may possibly be a metastable high temperature phase. Finding answers to these questions is part of ongoing research. Eventually, ways can be found to suppress either its formation or decomposition. As stated previously, this ternary alloy in theory should exhibit well-balanced creep, oxidation and fracture toughness properties. However, the two later properties have not been addressed so far and should be thoroughly assessed in future work, to explore the capability and applicability of a ternary eutectic Nb-Si-Cr alloys.

V. Acknowledgements

Financial support by the German science foundation (DFG) under grant no.'s HE1872/19-1 and -2 is gratefully acknowledged. Moreover, the authors would like to thank Frank Stein and Martin Palm from Max-Planck-Institut für Eisenforschung, Duesseldorf, Germany, as well as Georg Hasemann from Forschungszentrum Juelich for fruitful discussions on ternary eutectics. Moreover, support by the colleagues from Duesseldorf in terms of WDS measurements is gratefully acknowledged.

The authors would also like to thank Fabia Suess for experimental support. This work was partly carried out with the support of the Karlsruhe Nano Micro Facility (KNMF, www.knmf.kit.edu), a Helmholtz Research Infrastructure at Karlsruhe Institute of Technology (KIT, www.kit.edu). AK thanks the Carl Zeiss Foundation for financial support through a postdoc grant.

VI. References

[1] J.-C. Zhao, J. H. Westbrook, *MRS Bulletin* **2003** *(11)*, 622 – 630.
[2] B. P. Bewlay, M. Jackson, J.-C. Zhao, P. R. Subramanian, *Metall. Mater. Trans. A* **2003**, *34A (10)*, 2043 – 2052.
[3] F. Gang, M. Heilmaier, *JOM* **2014**, *66 (9)*, 1908 – 1913. DOI: 10.1007/s11837-014-1109-6.
[4] N. Sekido, Y. Kimura, Y. Mishima, *Mat. Res. Soc. Symp. Proc* **2003**, *753*, BB5.25.1-6.
[5] K. Zelenitsas, P. Tsakiropoulos, *Intermetallics* **2005**, *13 (10)*, 1079 – 1095. DOI: 10.1016/j.intermet.2005.02.002.
[6] J. Geng, P. Tsakiropoulos, G. Shao, *Materials Science and Engineering: A* **2006**, *441 (1-2)*, 26 – 38. DOI: 10.1016/j.msea.2006.08.093.
[7] J. Geng, P. Tsakiropoulos, *Intermetallics* **2007**, *15 (3)*, 382 – 395. DOI: 10.1016/j.intermet.2006.08.016.
[8] J. Geng, P. Tsakiropoulos, G. Shao, *Intermetallics* **2007**, *15 (3)*, 270 – 281. DOI: 10.1016/j.intermet.2006.06.003.
[9] B. Khazai, R. Kershaw, K. Dwight, A. Wold, *J. Solid State Chem.* **1981**, *39*, 395 – 400.
[10] G. Shao, *Intermetallics* **2005**, *13 (1)*, 69 – 78. DOI: 10.1016/j.intermet.2004.06.003.
[11] B. P. Bewlay, Y. Yang, R. L. Casey, M. R. Jackson, Y. A. Chang, *Intermetallics* **2009**, *17 (3)*, 120 – 127. DOI: 10.1016/j.intermet.2008.10.005.
[12] L. Cornish, D. M. Cupid, J. Gröbner, A. Malfliet, *Cr-Nb-Si Ternary Phase Diagram Evaluation*, http://materials.springer.com/msi/docs/sm_msi_r_10_010543_01 **2010**.
[13] J.-C. Zhao, M. Jackson, L. Peluso, *Acta Materialia* **2003**, *51 (20)*, 6395 – 6405. DOI: 10.1016/j.actamat.2003.08.007.
[14] P. Villars, L. D. Calvert, *Pearson´s handbook of crystallographic data for intermetallic phases: Vol. 3:* Cr_2Nb *-* $In_2P_3Se_9$, ASM International, Materials Park, Ohio **1991**.
[15] J. Geng, *Development of niobium silicide based in situ composites: Next generation materials for high temperature applications*, LAP Lambert Academic Publishing, Saarbrücken **2009**.

[16] B. Predel, *Nb-Si (Niobium-Silicon): Landolt-Börnstein - Group IV Physical Chemistry 5H Li-Mg - Nd-Zr*, Berlin, Heidelberg, http://materials.springer.com/lb/docs/sm_lbs_978-3-540-68538-8_2195 **1997**.

[17] M. E. Schlesinger, H. Okamoto, A. B. Gokhale, R. Abbaschian, *JPE* **1993**, *14 (4)*, 502 – 509. DOI: 10.1007/BF02671971.

[18] M. G. Mendiratta, D. M. Dimiduk, *Scr Metall. Mater.* **1991**, *25*, 237 – 242.

[19] B. P. Bewlay, C. L. Briant, A. W. Davis, M. R. Jackson, *Mat. Res. Soc. Symp. Proc* **2001** *(646)*, N.2.7.1-N.2.7.6.

[20] C. Seemüller, M. Heilmaier, T. Hartwig, M. Mulser, N. Adkins, M. Wickins, *Mat. Res. Soc. Symp. Proc* **2013**, *1516*, 317 – 322.

[21] P. R. Subramanian, T. A. Parthasarathy, M. G. Mendiratta, D. M. Dimiduk, *Scr Metall. Mater.* **1995**, *32 (8)*, 1227 – 1232.

[22] G. Brinson, B. B. Argent, *J. Inst. Met.* **1962/63** *(91)*, 293 – 298.

[23] K. S. Chan, *Materials Science and Engineering: A* **2002**, *337 (1-2)*, 59 – 66. DOI: 10.1016/S0921-5093(02)00011-4.

[24] G. A. Henshall, P. R. Subramanian, M. J. Strum, M. G. Mendiratta, *Acta Materialia* **1997**, *45 (8)*, 3135 – 3142.

[25] M. Yoshida, T. Takasugi, *Intermetallics* **2002**, *10 (1)*, 85 – 93. DOI: 10.1016/S0966-9795(01)00107-8.

[26] B. P. Bewlay, C. L. Briant, E. T. Sylven, M. R. Jackson, *Mat. Res. Soc. Symp. Proc* **2003** *(753)*, BB5.24.1-BB5.24.6.

[27] P. Jain, K. S. Kumar, *Acta Materialia* **2010**, *58 (6)*, 2124 – 2142. DOI: 10.1016/j.actamat.2009.11.054.

[28] D. Schliephake, M. Azim, K. von Klinski-Wetzel, B. Gorr, H.-J. Christ, H. Bei, E. P. George, M. Heilmaier, *Metall and Mat Trans A* **2014**, *45 (3)*, 1102 – 1111. DOI: 10.1007/s11661-013-1944-z.

[29] M. Heilmaier, M. Krüger, H. Saage, J. Rösler, D. Mukherji, U. Glatzel, R. Völkl, R. Hüttner, G. Eggeler, C. Somsen, T. Depka, H.-J. Christ, B. Gorr, S. Burk, *JOM* **2009**, *61 (7)*, 61 – 67. DOI: 10.1007/s11837-009-0106-7.

Tables

Table 1: Nominal and actual composition of the alloys used for triangulation. The numbers shown in Figure 2 are matched to the compositions accordingly.

alloy no.	nominal	actual (ICP-OES)
1	Nb-8.7Si-33.1Cr	Nb-9.0Si-33.3Cr
2	Nb-12Si-25Cr	Nb-12.5Si-26Cr
3	Nb-8.7 Si-22Cr	Nb-7.8Si-21.9Cr
4	Nb-12Si-33.1Cr	Nb-12.4Si-33.2Cr

Table 2: Quantitative EDS results for the ternary eutectic structures

alloy no.	alloy composition	Nb / at.%	Si / at.%	Cr / at.%
3	Nb-8.7Si-22Cr	60.7 ± 0.1	11.0 ± 0.5	28.3 ± 0.5
4	Nb-12Si-33.1Cr	60.7 ± 0.1	10.8 ± 0.6	28.5 ± 0.4

Table 3: Chemical composition of the phases in Nb-10.9Si-28.4Cr in the as cast state.

phase	Nb / at.%	Si / at.%	Cr / at.%
Nb_{ss}	84.6 ± 2.5	2.4 ± 0.8	13.0 ± 2.0
Cr_2Nb	39.9 ± 2.3	12.6 ± 0.9	47.5 ± 1.6
$Nb_9(Si,Cr)_5$	62.8 ± 1.3	16.2 ± 0.4	21.0 ± 1.6

Table 4: Chemical composition of the phases present in Nb-10.9Si-28.4Cr after heat treatment at 1500 °C for 100 h.

phase	Nb / at.%	Si / at.%	Cr / at.%
Nb_{ss}	89.9 ± 0.2	0.4 ± 0.1	9.7 ± 0.2
Cr_2Nb	33.8 ± 0.2	12.4 ± 0.3	53.7 ± 0.4
Silicide	60.5 ± 0.1	38.0 ± 0.2	1.5 ± 0.1

Figures

Figure 1: SEM-BSE micrographs of the alloys (a) Nb-12Si-25Cr and (b) Nb-8.7Si-33.1Cr, both in as cast condition

Figure 2: Partial liquidus projection of the Nb-Si-Cr system, including isothermal lines (calculated with PANDAT employing the PanNb database). Compositions according to the numbers are listed in Table 1. The red dots symbolize the nominal composition; blue ones represent the actual composition.

Figure 3: SEM-BSE micrographs of the alloys (a) Nb-8.7Si-22Cr and (b) Nb-12Si-33.1Cr. In both alloys ternary eutectic structures can be observed (marked with a red circle).

Figure 4: Micrographs of the ternary eutectic alloy Nb-10.9Si-28.4Cr: (a-b) SEM-BSE mode and (c) EBSD, false-color image of the phases Nb9(Si,Cr)$_5$ (yellow), Nbss (green) and Cr2Nb (red).

Figure 5: Indexed EBSD patterns of the phases present in Nb-10.9Si-28.4Cr: (a) Nbss, (b) Cr2Nb and (c) Nb9(Si,Cr)$_{5.}$

Figure 6: Phase evolution and stability in the alloy Nb-10.9Si-28.4Cr, starting from as cast state in (a) for different heat treatment conditions: (b) 1200 °C, 500 h; (c) 1300 °C, 100 h and (d) 1500 °C, 100 h.

Figure 7: Evolution of phase fraction and -size in Nb-10.9Si-28.4Cr for different heat treatment conditions. Average phase size determined by segmentation of BSE images is provided in brackets. Connecting lines are to guide the eyes.

Figure 8: indexed EBSD diffraction patterns showing the silicide phase evolution in Nb-10.9Si-28.4Cr for different heat treatment conditions: (a) Nb9(Si,Cr)$_5$ in as cast state and (b) α-Nb5Si3 after 1300 °C, 100 h

Figure 9: Stress dependence of the strain response for Nb-10.9Si-28.4Cr, shown as (a) strain rate vs. true plastic strain (deliberately stopped subsequent to minimum) and (b) minimum strain rate vs. true stress (Norton plot). Data marked with "*" were determined at 1000 °C.

Figure 10: Density-normalized Norton plot, showing the potential of Nb-10.9Si-28.4Cr when compared to other refractory metals based alloys as well as Ni-based superalloys.